Evolution of Persistent Wave Groups

JEROME A. SMITH

Scripps Institution of Oceanography, La Jolla, California

CORALIE BRULEFERT

Institut des Sciences de l'Ingénieur Toulon Var, Toulon, France

(Manuscript received 18 September 2008, in final form 10 August 2009)

ABSTRACT

During the near-field leg of the Hawaiian Ocean-Mixing Experiment (HOME-NF), short, steep surface wave groups were observed that elicited strong group-forced responses in the wave-filtered surface current field, as reported by Smith. Some of these wave groups persisted for 17 wave periods, yet were only about 1 wavelength long in the along-wind direction. Here, the authors consider the evolution of wave groups of the form observed and find that this persistence is consistent with linear dispersion in spite of the very compact form. The key aspects enhancing persistence are 1) that the wave crests within the group are oriented at an angle with respect to the group envelope and 2) they are much wider in the crosswind direction than along-wind (in the example examined in detail, about 5 times). According to a simplified model, groups with the observed 5-to-1 aspect ratio and this ''slant-wave'' structure can persist for up to 20 wave periods, consistent with the observations (cf. 8 periods for a collinear wave group). The maximum persistence increases in proportion to the across-wind length of the group.

1. Introduction

Motivation for this work comes from observations of large responses to passing wave groups reported by Smith (2006b). In brief, surface waves introduce a discrepancy between the mean speed measured at a fixed point (Eulerian mean) and the mean speed following an actual moving water parcel (Lagrangian mean); this difference is known as the ''Stokes drift'' (after Stokes 1847). Integrated over depth, the ''Stokes transport'' varies roughly as the square of wave amplitude, so wave groups have an associated varying mass transport. The convergence and divergence of this wave-induced mass transport must be compensated for by an ''underlying flow response'' in the Eulerian (fixed frame) mean flow field. The depth over which the compensating flow arises is proportional to the distance between the convergence and divergence. The longer the group, the deeper the return flow and the weaker the surface value of the response should be for the same net transport. The shortest group is one wave long, for which the expected surface response should be about half the surface Stokes drift (e.g., Longuet-Higgins and Stewart 1962; Smith 2006a). However, Smith (2006b) found a response roughly equal to the Stokes drift at the surface, about double the expected value (this remains unexplained).

In addition to the larger than expected response, it was noted that the wave groups responsible for inducing the response were both short, of order one wavelength, and persistent, lasting sometimes for more than 2 min (17 wave periods) before propagating out of view. Smith (2006b) focused on the forced response of the underlying flow to the groups, comparing it to the theoretical response as noted previously, but deferring examination of the wave groups themselves. Here, we take up this examination. A key question is how long such wave groups ought to last according to linear theory, and hence whether the explanation requires nonlinear dynamics.

Previous works on nonlinear deep-water surface wave groups have focused mainly on long groups, so weakly nonlinear effects have time to develop. On one hand, modulational instabilities can cause a uniform wave train to develop into ''groups'' (e.g., Benjamin and Feir 1967; Longuet-Higgins 1978; Dysthe 1979); and on the other,

Corresponding author address: Dr. Jerome A. Smith, Mail Code 0213, 9500 Gilman Dr., La Jolla, CA 92093-0213.
E-mail: jasmith@ucsd.edu

DOI: 10.1175/2009JPO4149.1

groups can evolve to exceptionally steep waves that persist only briefly, producing ''rogue waves'' or breaking (e.g., Tulin and Waseda 1999; Banner and Peirson 2007; Dysthe et al. 2008). In contrast, the wave groups discussed here are exceptionally short (on the order of one wavelength) but persist for many wave periods without changing significantly in structure or form. In further contrast to most previous theoretical treatments of wave groups (an exception is noted below), the constituent waves are not aligned with the group envelope. Indeed, these observed groups resemble short pieces of ship's wakes, which have been shown to persist a very long time and are thought to eventually involve nonlinear dynamics (e.g., see Brown et al. 1989). However, it is not clear that these results apply to a short piece of a ship's wake, rather than an essentially infinitely long one.

Here, the interest lies in how long wave groups of the form observed ought to persist, compared to how long they actually do. We explore first the hypothesis that nonlinear dynamics are not required; that is, whether the observed persistence is consistent with linear propagation. We find the persistence is in fact compatible with linear dynamics, largely because of how the waves composing the group are oriented at an angle relative to the group envelope, which is narrow in one direction but long in the other.

First, we briefly review the experimental setting, instrumentation, and analysis methods. We show a representative example of a compact persistent wave group, which lasts for about 120 s (17 wave periods). We then show that linear propagation is sufficient to explain the persistence, given the actual (measured) surface wave field at a nominal starting time, and using linear dispersion to forward propagate the field in time. The comparison with the later observed data is quite good. Next, we develop a simple model of a wave group with waves that are slanted at an arbitrary angle with respect to the group envelope and find that persistence can be explained as a consequence of this structure. Then, we return to the group-forced response as a useful proxy for the occurrence of such short, steep, and persistent wave groups. The results indicate they are surprisingly common at this site, with typically 2–3 such groups per 8.5-min segment, whenever (but only when) the wind blows. Since the winds were either calm or blowing at about 10 m s^{-1}, this also reinforces the link between these short, steep, and persistent waves and the wind: group speeds of 5 m s^{-1} imply phase speeds of about 10 m s^{-1}, corresponding to the expected ''wind wave peak.'' Finally, we discuss what aspects of the conditions may be conducive to forming such groups and list some possible effects.

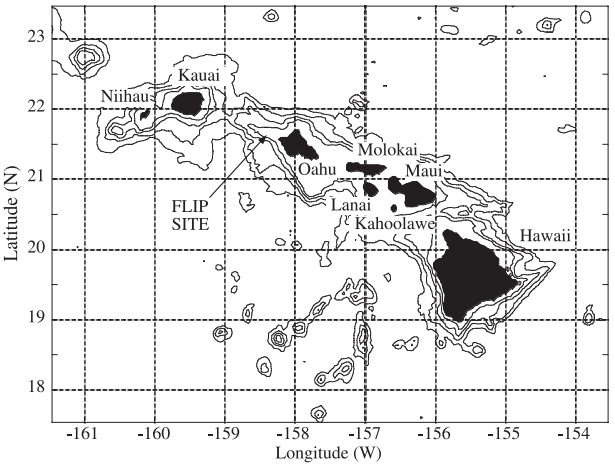

FIG. 1. Location of R/P *FLIP* during HOME-NF, September–October 2002. The site is about 30 km west of Oahu in about 1000-m water depth, over an underwater ridge that extends roughly halfway to Kauai. Depth contour interval is 1000 m; the deepest shown is 4000 m (figure from Smith 2006b).

2. Experimental setting and data

Quantitative estimation of the directional surface wave field requires data that are extensive in both time and space: direction, wavelength, and frequency must be resolved over a wide range of scales. To provide this, a 50-kHz long-range phased-array Doppler sonar (LRPADS) was operated continuously for about 20 days, from 14 September to 5 October 2002. The data were gathered aboard the research platform–floating instrument platform (R/P *FLIP*), in conjunction with the near-field leg of the Hawaiian Ocean-Mixing Experiment (HOME-NF). The R/P *FLIP* was moored over the Kaena Ridge just off Oahu, Hawaii, where the water depth is about 1000 m, increasing to well over 4000 m off either side of the ridge (see Fig. 1).

In addition to the LRPADS data, many other measurements were made from R/P *FLIP*. These include wind, surface wave elevation spectra, and conductivity, temperature, and depth (CTD; with which salinity and density can also be calculated) profiling every 4 min or so throughout HOME-NF (e.g., see Pinkel and Rudnick 2006; Klymak et al. 2008).

The general design and operation of a PADS is described in Smith (2002) and the extension to the LRPADS is summarized in Smith (2006b). The brief description here follows the latter. For the LRPADS, as configured in HOME-NF, a pie-shaped area extending out to 1.5 km in range and 44° in bearing is segmented into measurement bins about 1.3° wide (33 beams) and 7.5 m in range (200 range bins), a total of 7000 locations. The area is sampled every 2.5 s, which is the time needed for sound to propagate out 1800 m and back. Vertical

location is not resolved; the vertical beamwidth includes the surface bubble layer beyond about 90-m range, so the effective location of the measurements is dictated by the centroid of the bubbles, which are some 10^4 times brighter than competing scatterers. Since bubbles are strongly surface trapped (Thorpe 1986; Crawford and Farmer 1987), the measurements can be considered as essentially surface velocities. Horizontal (azimuthal) beamforming is done via time delay, since the array is wider than the transmitted ''code bits'' (the 0.1-ms code bits are 15 cm long, and the array is over 1 m wide). The raw data stream was segmented into files of roughly 8.5 min each and processed later. After beamforming, the Doppler shift is estimated with a time-lagged covariance technique, treating each ping independently (Rummler 1968). This yields a finite level of Doppler noise, even at a high signal-to-noise ratio (SNR); here, repeat-sequence codes were used (Pinkel and Smith 1992), reducing the single-ping rms noise level to about 7 cm s^{-1} per range and angle bin (see also the discussion, section 6). At the farthest ranges, the SNR decreases as the signal fades into the ambient acoustic noise, further degrading the estimates. Here, we taper the data to zero to facilitate FFT processing, stopping short of ranges where the ambient noise is an issue, even when ships or other noise sources are present.

The LRPADS provides both surface waves and the underlying surface flows over a sizeable area, with continuous coverage in both space and time. The resolution is sufficient to clearly define waves with periods longer than 5 s, and the area is large enough that with 10 m s^{-1} winds the equilibrium peak waves (7-s period) can be observed for many periods: waves with phase speeds of 10 m s^{-1} have group speeds of 5 m s^{-1}, with a 1-km aperture, it would take 200 s (or 28 wave periods) for a group to cross the area. The ability to track many wave groups with such precision over such long times is fairly novel, particularly on the open ocean.

The continuous 3D coverage (2D space and 1D time) permits clean separation of the observed variability into different dynamical phenomena, with a variety of methods to choose from (e.g., see Smith 2002, 2008). The approach taken here is to filter by phase speed. Surface waves are the fastest modes measured and so are easily separated from embedded flow features, such as Langmuir circulation, fronts, or the previously mentioned Eulerian response to the passing wave groups themselves (as noted in Smith 2006b, the last in particular depends on the full 3D coverage for accurate separation). After this separation, the well-constrained characteristics of surface gravity waves permit the directional response of the LRPADS (which provides only one component of surface velocity along each beam) to be largely compensated for (described in section 3). This permits surface wave propagation and evolution to be considered independent of angular position across the measurement area.

As noted, a previous analysis of this dataset revealed a surprisingly prominent Eulerian response to passing groups (Smith 2006b), which also provides motivation to consider the wave groups themselves, as we do here. Specifically, we consider the linear dynamics and evolution of the wave groups as observed, which can be quite short in the along-wave direction (about 1 wavelength), yet remarkably persistent, having been observed to last over 17 wave periods. We shall consider a particular representative example in some detail to help determine the controlling dynamics.

A useful way to view wave propagation is via contours of velocity plotted on a time–range (T–R) plane (''T–R plot,'' as in Fig. 2) Distinct wave groups appear as diagonal bands of higher-amplitude velocities, within which the phase speed can be perceived as the more steeply angled crests and troughs of the waves. The group circled in Fig. 2, which persists for about 120 s, is our chosen example. Since the waves composing the group have about a 7-s period, this corresponds to about 17 wave periods.

The spectrum of waves has several peaks in direction and frequency, a couple of which confuse the picture yet do not interact with the wave groups of interest. For clarity, the data in Fig. 2 were filtered for outgoing (roughly downwind) waves only, suppressing some large upwind-propagating swell (the full 2D wavenumber spectrum is shown later).

3. Data processing methods

a. Fourier transform processing: Time–range to frequency–wavenumber

A fast Fourier transform (FFT) in time yields both positive and negative frequencies that are complex conjugates of each other and so redundant. The FFT can be used to generate an imaginary component of the original times series by setting all negative frequencies to zero, increasing the positive frequency coefficients by the factor of $2^{1/2}$ to preserve the variance, and then doing the inverse transform. The result yields both the original series (as the real part) and a Hilbert transform (as the imaginary part; see, e.g., chapter 13 in Bendat and Piersol 1986). This synthesized imaginary part effectively incorporates temporal information into each spatial snapshot, so the direction of propagation of each wavenumber component (e.g., from a 2D spatial FFT) is unambiguous: for an input (real) cosine in space, the synthesized

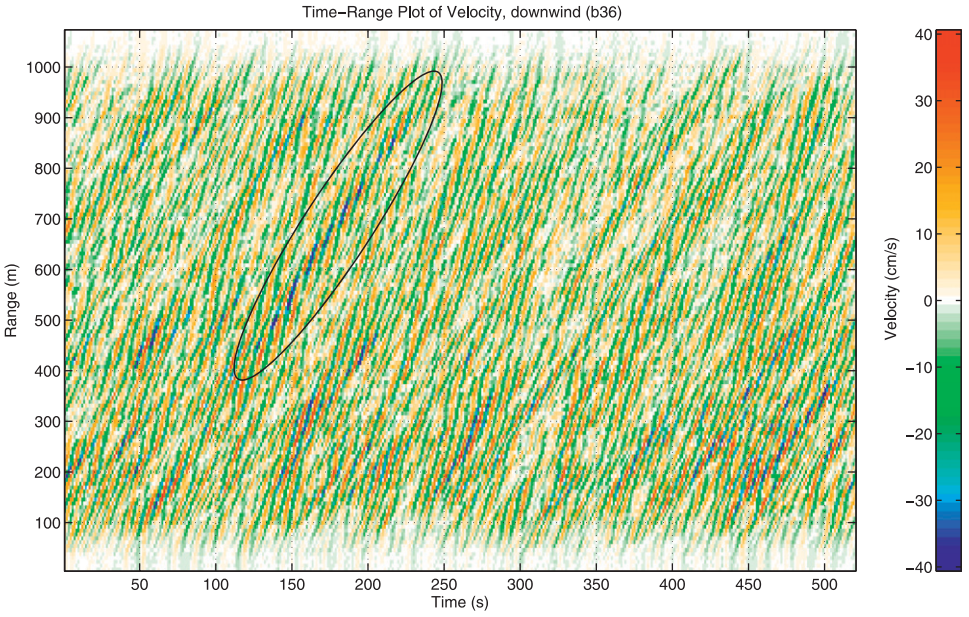

FIG. 2. An example T–R plot of surface velocity along a single sonar beam. Note the appearance of wave groups (groups of higher-amplitude waves), such as the one circled. This group, which lasts about 120 s (from $t \approx 110$ to 230), is selected for closer study.

imaginary part can be either −sine (corresponding to waves going one way) or +sine (going the other way)—the temporal evolution determines which (or how much of each). This permits each snapshot to be processed independently, with no ambiguity in direction, as would occur with only a single original (all real) snapshot.

Working from the temporal FFT data (frequency transform), a spatial FFT can be performed along each sonar beam, using a finite-range interval of dependably good data, which we take here as 100–950 m (this rather short end point insures that the signal will dominate even over the occasional noisy boat traffic). The result is a two-dimensional (2D) Fourier transform from time and range to frequency and wavenumber (see Fig. 3). A notable feature of this 2D spectrum is that the upper half (outgoing waves) has a much larger area of high wave energy; these correspond to approximately downwind-traveling waves. Further, it is pretty clear that the branch of wave energy in this upper half, which extends past the Nyquist frequency, corresponds to genuine higher-frequency waves (the Nyquist frequency is that for which there are 2 samples per cycle; with 2.5 s per sample, the Nyquist frequency is 0.2 Hz). The downwind surface wave variance is very large, even in the high-frequency "tail" of waves beyond 0.2 Hz. It is important to prevent this tail of energy in the upper-right quadrant of Fig. 3 from aliasing into the lower-left quadrant of the spectrum, where it would be misinterpreted as lower-frequency upwind-traveling phenomena of some sort. To prevent this, we cut the lower half off short of the Nyquist frequency, along the solid, blue line shown in Fig. 3. Smith (2006b) discusses the option of keeping the upper-high-frequency tail beyond the Nyquist frequency by artificially doubling the frequency range and "dealiasing" to favor this downwind branch (e.g., along the continuation of the solid, blue line); however, in the present analysis, the important wave periods are on the order of 7 s, so this is unnecessary. As noted in Smith (2006b), it appears we could examine waves in this way beyond 0.3 Hz, provided all the conditions are met to say with confidence that the correct "branch" is positively identified (e.g., this would not be true of a sonar beam directed anywhere near perpendicular to the wind).

b. Correcting for the directional response of the array

Each sonar beam measures just the along-beam (radial) component of the surface velocity. As deployed in HOME-NF, this corresponds to a horizontal component of the orbital velocities of the waves, sampled along the line of the beam. The response to a plane wave propagating at an angle θ relative to a particular beam is reduced by $\cos\theta$ compared to a similar wave traveling straight along the beam (either directly toward or away from the instrument). To estimate wave elevations, for example, requires that we correct for this to the extent possible. Here, we outline a method to apply a correction using the wavenumber–frequency (k–f) transform of the time–range data from a single beam at a time. The

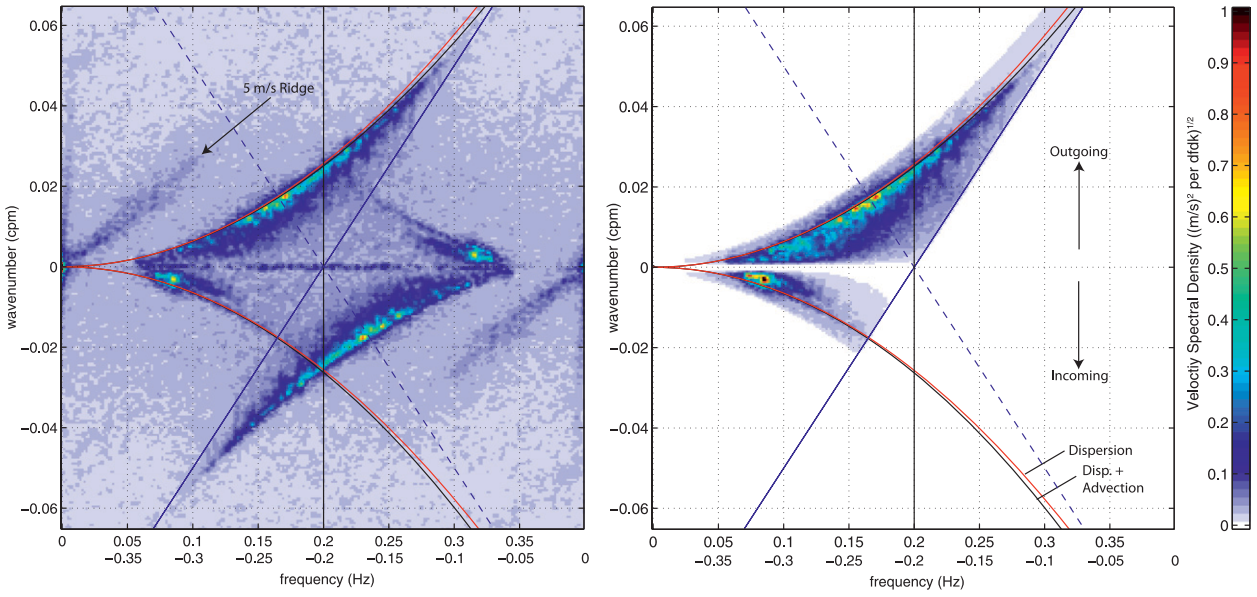

FIG. 3. A typical *k–f* spectrum from the LRPADS data. (left) The complete spectrum with + and − frequencies and aliasing. Note the straight ridge of variance at a slope corresponding to 5 m s^{-1}. (right) The surface wave–related part of the spectrum, which has maxima along a curve that is roughly quadratic in *f*. The red curves correspond to linear dispersion, while the black curves are corrected for advection by the observed mean current. The outgoing waves (upper half) go more nearly downwind, so the wave variance is larger on that half of the spectrum. The bottom half (incoming waves) was zeroed out to make Fig. 2. The wave part on the right was partially corrected for the directional response (see text), so the wave variance extends closer to zero wavenumbers than in the left (look particularly near 0.1 Hz). To prevent aliasing of the high-frequency waves into slower upwind-propagating bogus variance, the lower half is cut at the solid blue line rather than at the Nyquist frequency (0.2 Hz). In circumstances where there may be strong incoming waves as well as outgoing, we would cut the upper half in a similar way, along the blue dashed line.

method is essentially as described by Smith (2006b), with a minor improvement minimizing the expected error.

We begin with the 2D frequency–wavenumber (*f–k*) transform from the time–range data of a single beam at a time; subsequently, we will combine information from all the beams to get the complete 2D spatial picture. The components $U_r(f, k_r)$ are the Fourier coefficients from the time–range FFTs of the observed radial velocities $u_r(t, r)$ along a given sonar beam. Then, in the surface wave part of the spectrum, at each frequency *f* the radial component of a wavenumber is $k_r = k_f \cos\theta_k$, where $k_f = k(f)$ is the magnitude of the true wavenumber, which we will estimate from the linear dispersion relation, and θ_k is the angle of propagation relative to the beam of the wave corresponding to k_r. In the presence of a mean current *V*, the deep-water linear dispersion equation for surface gravity waves is

$$\omega = (g\kappa)^{1/2} + \kappa V \cos(\theta_k - \theta_V) \tag{3.1a}$$

or

$$f = \left(\frac{gk}{2\pi}\right)^{1/2} + kV\cos(\theta_k - \theta_V), \tag{3.1b}$$

where *f* is the wave frequency in Hz (and ω is in rad s^{-1}), *k* the wavenumber magnitude in cycles per meter (cpm; and κ is in rad m^{-1}), *V* is the mean current magnitude, and θ_V is the direction of the current (also relative to the beam direction). This can be inverted for $k(f)$ in a form that is well behaved as $V \to 0$ (Smith and Bullard 1995):

$$\begin{aligned} k_f &= k(f) \\ &= (8\pi g^{-1})f^2\{1 + [1 + (8\pi g^{-1})fV\cos(\theta_k - \theta_V)]^{1/2}\}^{-2}. \end{aligned} \tag{3.2}$$

In general, the currents are small compared to the wave phase speeds. For example, a 3-s period wave has a phase speed $c = \omega g^{-1} = 2\pi f g^{-1}$ of about 4.7 m s^{-1}, while the typical currents are 0.20 m s^{-1} or less, so $V/c \approx 0.04$. In terms of the small normalized current $\hat{V} \equiv V/c$, (3.2) simplifies to

$$k_f \approx k_0[1 - 2\hat{V}\cos(\theta_k - \theta_V)], \tag{3.3}$$

where $k_0 = (2\pi g^{-1})f$ is the zero current value for *k*. Although this correction is small, it is large enough to see on the *k–f* spectral plots (see Fig. 3). It is also cumulative and so becomes noticeable after the waves propagate for 100 s or more, as we hope to test here.

To estimate, for example, wave elevations from the measured radial component of velocities $U_r \approx U_0 \cos\theta_k$

(where U_0 is the true wave orbital velocity), U_r must be effectively divided by the response $\cos\theta_k = k_r/k$; however, this is singular near the $k_r = 0$ axis. In Smith (2006b), a weighting function was introduced to tame this singularity. Here, we improve on this by forming an optimal estimate of $U_r/\cos\theta_k$ in the presence of noise. Let the observed velocity be the sum of the true value plus a uniform variance zero-mean noise term ε (the Doppler estimation noise is distributed uniformly on the f–k plane, so this is appropriate):

$$U_r = U_0(f, k_r)\cos\theta_k + \varepsilon = 2\pi f A(f, k_r)\left(\frac{k_r}{k_f}\right) + \varepsilon, \tag{3.4}$$

where k_f is the wavenumber magnitude from dispersion, k_r is the wavenumber component as measured along the sonar beam under consideration, θ_k is the angle between the beam direction and the wave propagation direction, and $A(f, k_r)$ is the (complex) elevation amplitude of the component with frequency f and along-beam wavenumber component k_r. Then, we seek an optimal weight b such that the estimate $\hat{U} \equiv bU_r(f, k)$ has minimal error relative to the true U_0 (which we also know is in the direction of wave propagation at the crests):

$$\langle|\hat{U} - U_0|^2\rangle = \langle\hat{U}^2\rangle - 2\langle\hat{U}U_0\rangle + \langle U_0^2\rangle = \text{minimum}. \tag{3.5}$$

The result (setting the variation with respect to b to zero) yields an optimal estimate:

$$b = \frac{q}{q^2 + \langle\varepsilon^2\rangle/\langle U_0^2\rangle}, \tag{3.6}$$

where $q = \cos\theta_k = k_r/k_f$. The orbital velocity variance $\langle U_0^2\rangle$ is related to the elevation variance as $U_0^2 = \omega^2 A^2(f) = (2\pi f)^2 A^2(f)$, so if the elevation frequency spectrum has the form $\langle A^2(f)\rangle \propto f^{-5}$ (e.g., as in the ''equilibrium range'' of Phillips 1958), then $\langle U_0^2\rangle \propto f^{-3}$. To avoid specifying both the waves' orbital variance and the noise level explicitly, we instead specify a ''critical frequency'' f_C at which $\varepsilon^2 = U_0^2(f_C)$. Then, since $\langle U_0^2\rangle \propto f^{-3}$, it follows that $\langle\varepsilon^2\rangle/\langle U_0^2\rangle = (f/f_C)^3$. Since the peak waves generally exceed the extrapolated value of this ''equilibrium-range'' level (e.g., Hasselmann et al. 1973), this is a conservative estimate of the signal-to-noise ratio for the peak wind waves of interest here, which is acceptable. We estimate the critical frequency by noting where the surface wave–related ridge on the measured k–f spectrum fades into the background. For example, on the upper (downwind) branch in Fig. 3, this occurs near $f =$ 0.32 Hz. In terms of this critical frequency, the optimal weight is

$$b = \frac{q}{q^2 + (f/f_C)^3}. \tag{3.7}$$

Although each individual beam is ''blind'' to waves propagating at a right angle to the beam direction, the beam directions over the whole field of view vary over 44°, so the array taken together can detect waves going in any direction to some degree.

A useful way to characterize the resulting directional response is to specify where the practical weight b is just half as large as the ideal weight $1/q = 1/\cos\theta_k$. This is just where $\frac{1}{2} = bq = q^2/[q^2 + (f/f_C)^3]$, or $q = (f/f_C)^{3/2}$. For example, with $f_C = 0.32$ Hz, the 7-s-period group waves have a critical-frequency ratio f/f_C of about $1/2.25 = (1/1.5)^2$, so the response is half as large as ideal at $q = (1.5)^{-3}$ or for θ_k about 17° short of 90°. At this frequency then, waves propagating within 73° of parallel to the axis of the pie (the center angle) have at least half the beams with a response factor of better than ½. Here, the focus is on waves and groups propagating roughly downwind, hence within 45°–60° of being directed along the axis of the pie. Thus, for this study no additional correction is applied beyond the previously described optimal weight.

The optimal weights can be defined separately for the waves propagating away (k_r positive) versus toward R/P *FLIP* (k_r negative). This permits choosing different values of f_C for downwind versus upwind waves. Also, note that the sign of approaching waves' orbital velocities are reversed (in accordance with $\cos\theta_k$ being negative), so in all cases the resulting estimate $\hat{U}$ corresponds to a velocity that is directed toward the estimated true wavenumber direction at the crest. Thus, for example, dividing the estimated $\hat{U}(f, k_r)$ by the corresponding frequency $\omega = 2\pi f$ results in proper estimates of elevation $\zeta(f, k_r)$. When working from a single snapshot, the frequency is recovered from the wavenumber via the dispersion relation in (3.1).

Figure 4 shows the example velocity fields corrected for the directional response, with the actual velocity field (real part of the complex velocity) on the right and the envelope (complex magnitude) on the left.

4. Linear propagation model

As noted, the ''positive frequency only'' FFT processing incorporates directional propagation information implicitly into the spatial maps of (now complex) velocity in each snapshot (time sample). Thus the 2D spatial map of complex velocities can be processed independently for each snapshot without directional ambiguity.

The simplest model for wave evolution is based on linear propagation of each wavenumber component (see, e.g., section 11.2 in Whitham 1974). Here, this is implemented

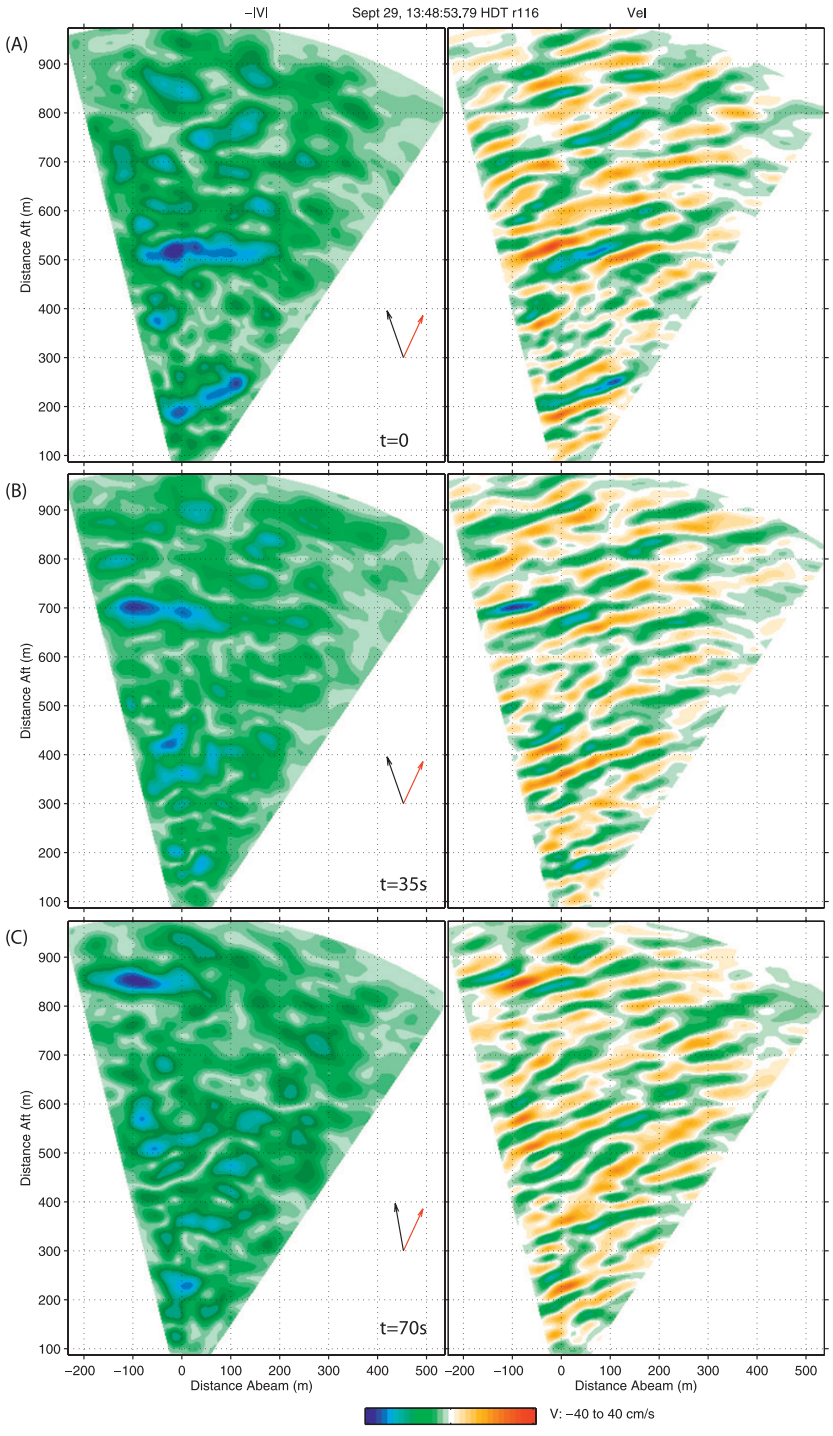

FIG. 4. A series of snapshots showing wave propagation. (left) The wave envelope (plotted negative for better color) and (right) the orbital velocity field. The black arrows show wind direction and speed (~10 m s^{-1}), and the red show the mean surface current (~8 cm s^{-1}). (a) The ''initial snapshot'' for the linear propagation test (see text), this shows both a ''slant-wave group'' (near 500-m range) and a ''collinear wave group'' (near 200 m). Note that (right) the wave crests in the lower group are nearly parallel to (left) the envelope, while the upper group has crests slanted at an angle with respect to the envelope orientation. (b) 35 s later (5 wave periods), the lower group has dispersed, while the upper group continues. (c) After 70 s (10 wave periods), the slant-wave group still persists. The orientations of the images have all been rotated ~10° so the long dimension of the persistent group is aligned with *y* (left to right).

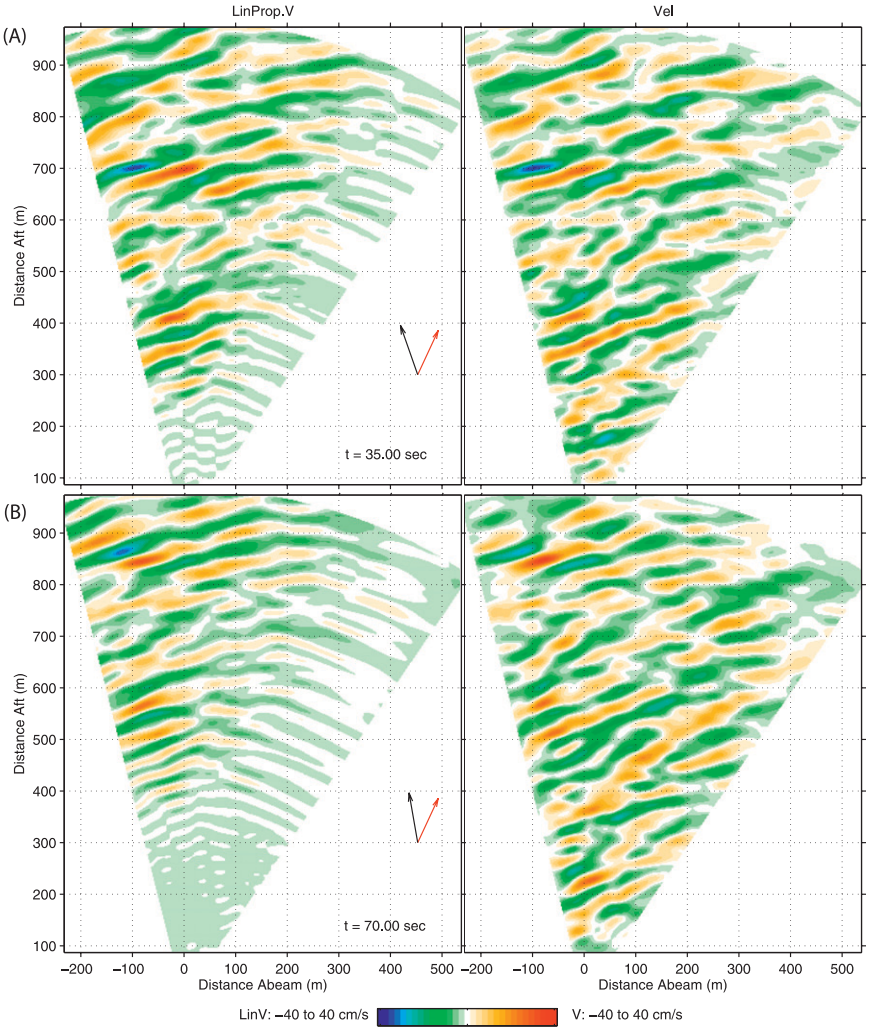

FIG. 5. Comparison between (left) linear propagation and (right) the real observed propagation after (top) 5 wave periods and (bottom) 10 wave periods. The initial snapshot is shown in Fig. 4a. The propagated data look like the real data in the upper-left areas, following the persistent wave group. The lower-right part of the pie becomes calm in the linear propagation model as zero-amplitude waves propagate into the field of view through the boundary. Arrows as in Fig. 4.

with complex sinusoidal behavior in both time and space: the frequency is deduced via linear dispersion from the wavenumber, which is derived from a spatial 2D FFT of the (complex) velocity field. As before, the area-mean current is incorporated in the dispersion relation for $f(k)$ [Eq. (3.1b)]. Although this advection is small, it can have a noticeable effect over the 100-s life span of the wave groups: a 20 cm s^{-1} current would result in a 20-m offset after 100 s, a significant fraction of the order of a 70-m group length.

To implement linear propagation, we start with an initial snapshot at some time t_0 (e.g., the top panel of Fig. 4), take the 2D spatial FFT of the complex velocities, propagate each component forward in time by multiplying each complex wavenumber component by the corresponding factor $\exp[-i2\pi f(k)(t - t_0)]$, and inverse FFT. We then compare the propagated field with the observed one at later times (we could also compare earlier times). Figure 5 shows both the propagated and observed velocity fields (real parts), while Fig. 6 shows the corresponding wave envelopes (complex magnitudes), all starting from the initial snapshot shown in the top panel of Fig. 4. Only the area where linear propagation has a fair chance should be compared (i.e., ever more to the upper-left corner, since zeroes propagate in from the bottom and right).

In both the real data and the linear propagation results, we observe that there are two kinds of wave groups:

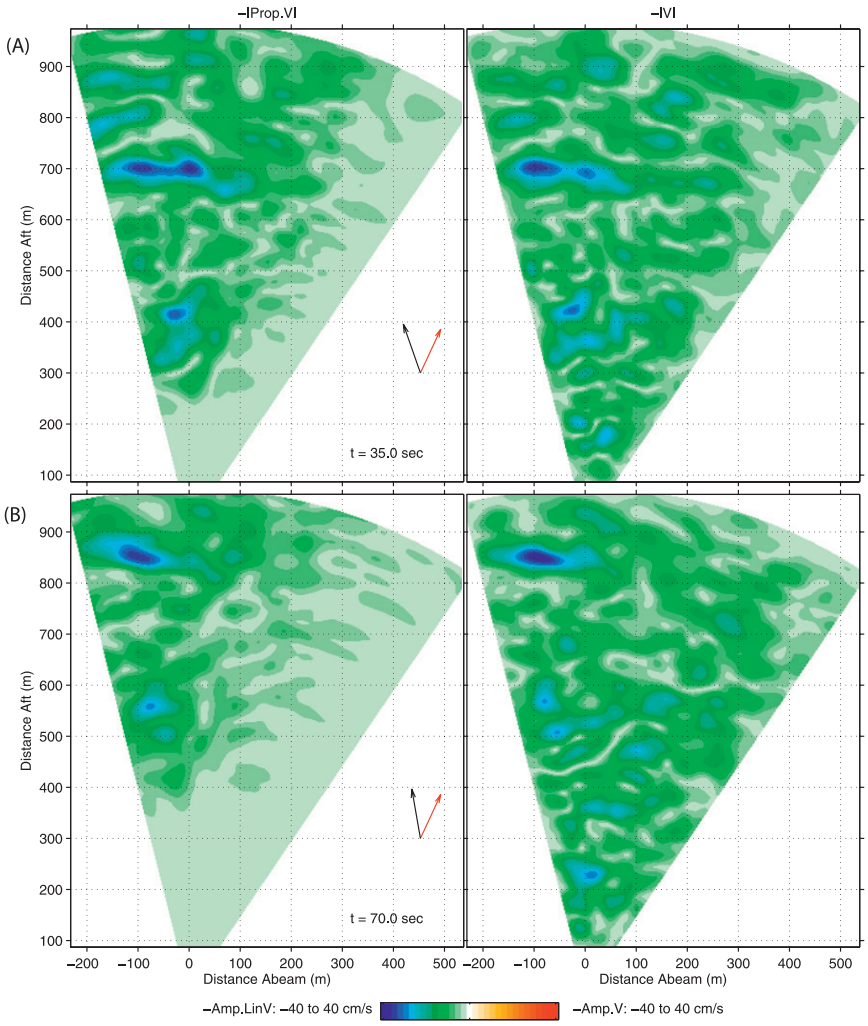

FIG. 6. As in Fig. 5, but showing the wave envelopes (plotted with the negative color scale, consistent with Fig. 4). (left) The linear propagation results and (right) observed waves after (top) 5 and (bottom) 10 wave periods show good agreement in the upper-left area where the propagation has a fair chance. The initial snapshot is shown in Fig. 4a. Arrows indicate wind (black) and current (red), as in Figs. 4 and 5.

1) One kind of group (seen near 200-m range at the bottom of the pie in Fig. 4) disperses quickly. The waves inside the group are aligned with the envelope (i.e., the crests are roughly parallel to the long axis of the envelope).
2) The other kind of group (starting near 500-m range in Fig. 4) has an envelope narrow in "x" (vertical) and long in "y" (left to right), but has waves inside that propagate at a finite angle φ with respect to the group envelope orientation and persists.

We focus on the latter, the "persistent wave group." What accounts for the endurance of this group? There are three kinds of explanations (not mutually exclusive): 1) the superposition of independent wave components obeying linear dispersion, but with waves that are slanted at an angle with respect to the group envelope (a "slant-wave group"), 2) nonlinear dispersion and/or wave–wave interactions, and 3) advection and straining by the underlying forced response.

As seen in Figs. 5 and 6, the difference between the propagated velocity fields and the observed velocity fields are small. For the persistent group, we find that the velocity variance matches to better than 10% even after 10 wave periods (70 s), using a 400-m square box centered on the group. Further, there is no apparent bias in the phase of the propagated waves versus the observed ones (which is easy to quantify with complex values)—the errors appear more or less random. Thus, the real propagation speed matches the linear value to within

our resolution (say within a half a range bin, or ±3.75 m over the 70-s propagation time, or 5 cm s^{-1}). The propagated wave group envelope remains as tight as the observed one, indicating linear dynamics are sufficient to explain these short, steep, and persistent wave groups. The first explanation is the simplest and fits the data we have, so it is preferred. As an aside, the second and third explanations—the nonlinear dispersion correction and advection by the forced group response, respectively—have opposing tendencies and so (partially) cancel. This may help explain why linear dispersion works so well, even after the times long enough to see subtle errors in the propagation speed. This also means that nonlinear interactions may still play a role in the group persistence; therefore, they are not ruled out.

We next use some characteristic values of this observed persistent group to examine and understand its behavior in terms of a simplified (but more generalized) model wave group.

5. Group evolution and dispersion

Consider the linear propagation of a model wave group in which the waves composing the group are at an angle φ relative to the group envelope orientation—a slant-wave group. First, orient the axes so the long dimension of the observed group lies parallel to the y axis ($+y$ to the left), the group is short in the x direction ($+x$ upward), and the angle φ is reckoned from the x axis (+ angle is to the left of up).

To help introduce the concept, first consider a simple sum of two waves of amplitudes a and b (e.g., for elevation), with slightly different values of the x component of (radian) wavenumber κ_x, no difference in the y-component κ_y, and a corresponding difference in frequency ω:

$$\begin{aligned}\zeta(x, y, t) &= \mathrm{Re}\{ae^{i(\kappa_x x+\kappa_y y-\omega t)} + be^{i[(\kappa_x+\Delta\kappa_x)x+\kappa_y y-(\omega+\Delta\omega)t]}\} \\ &= \mathrm{Re}\left\{ae^{i(\kappa_x x+\kappa_y y-\omega t)}\left[1+\left(\frac{b}{a}\right)e^{i(\Delta\kappa_x x-\Delta\omega t)}\right]\right\}.\end{aligned} \tag{5.1}$$

Taylor expanding $\Delta\omega \approx \Delta\kappa_x(\partial\omega/\partial\kappa_x) = \Delta\kappa_x c_x^g$, the envelope factor on the second line is seen to propagate at roughly $c_x^g \equiv \partial\omega/\partial\kappa_x$:

$$\left[1+\left(\frac{b}{a}\right)e^{i(\Delta\kappa_x x-\Delta\omega t)}\right] \approx \left[1+\left(\frac{b}{a}\right)e^{i\Delta\kappa_x(x-c_x^g t)}\right]. \tag{5.2}$$

Since the real wave group envelope is much narrower in x than y, we anticipate that the wavenumber spread is dominated by $\Delta\kappa_x$, similar to this simple superposition example (where $\Delta\kappa_y \to 0$). Even though the waves propagate at an angle to the x axis, the group envelope is long in y and short in x, and its major axis is roughly parallel to the y axis, so $\Delta\kappa_x \gg \Delta\kappa_y$.

What is observed in the data is a wave group envelope that propagates at about 5 m s^{-1} in the x direction (vertical in Figs. 4–6; however, note that the group does drift a bit to the left as well). In all these figures, the pie plots are rotated (~10°) so that the persistent wave group's envelope is oriented with the long dimension parallel to y, consistent with the axis orientation defined previously. The group length in the x direction is about 70 m, roughly 1 wavelength at the center wave period of about 7 s, and is about 5 times that in the y direction.

We shall start with a model wave group and estimate how quickly it disperses with time. It's useful to first define and examine a curve on the wavenumber plane showing all waves that have an x component of group velocity c_x^g matching the observed group propagation speed in that direction. Figure 7 shows the full 2D wavenumber spectrum corresponding to the data shown in Figs. 4–6 for an area immediately surrounding the persistent wave group (400 m by 400 m, centered on the group), including upwind and crosswind swell peaks that were filtered out for Figs. 4–6 (where they would have confused the view of the wave groups of interest). Figure 7 also shows a roughly oval curve representing the wavenumbers for which $c_x^g = 5$ m s^{-1}. The center wavenumber of the group is assumed to lie near this curve. The spread in wavenumber is dominated by $\Delta\kappa_x$ (or Δk_x in cpm, as annotated in the figure). To make our initial estimates, we set $\Delta\kappa_x$ and $\Delta\kappa_y$ using length scales estimated from Fig. 4:

$$\Delta\kappa_x = \frac{2\pi}{L_x} \quad \text{and} \quad \Delta\kappa_y = \frac{2\pi}{L_y}, \tag{5.3}$$

where $L_x \approx 70$ m and $L_y \approx 5L_x \approx 350$ m.

Since the x-wise width of the group envelope L_x is roughly a wavelength, it follows that $\Delta\kappa_x \approx |\kappa|$. The spread of peaks in the x direction in the actual estimated 2D wavenumber spectrum (Fig. 7; excluding upwind waves) is consistent with this. Note too that the "center wavenumber" is closely aligned with the wind direction. It might be more appropriate to think of the group envelope as being "slanted" rather than the constituent waves. As seen in the propagation exercise, the group moves up and to the left (Figs. 4, 5, and 6), consistent with going directly downwind.

To estimate a group dispersal time, we take the time needed for the spread in component group velocities to separate the fastest and slowest components by the corresponding distances L_x or L_y. Then the "x wise" and "y wise" dispersal times are roughly

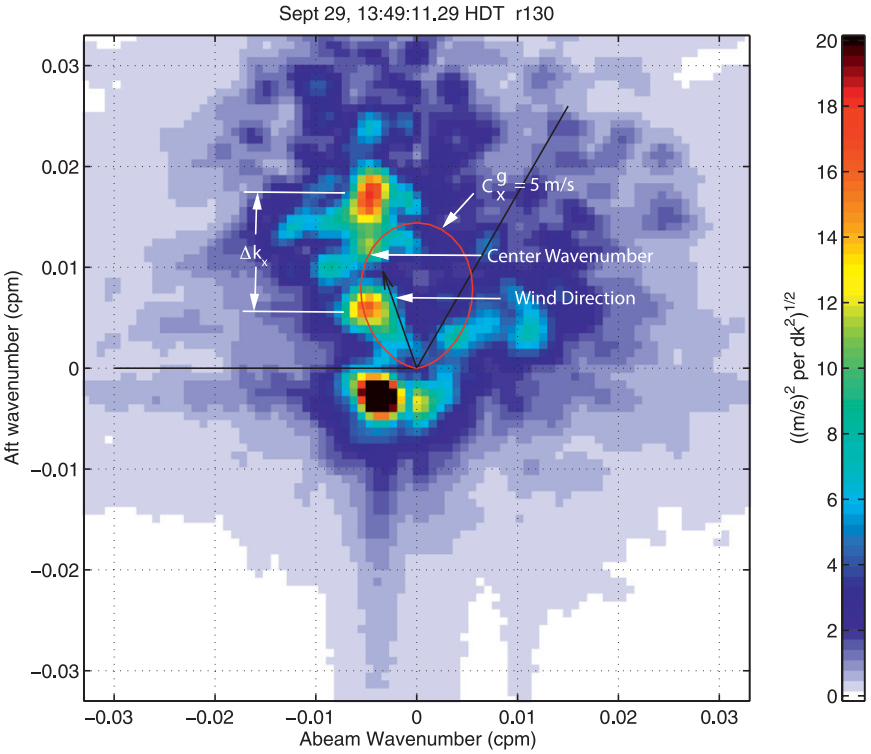

FIG. 7. The 2D wavenumber spectrum corresponding to the times illustrated in Fig. 4, using a box 400 m on a side centered on the persistent group. The roughly oval red curve shows all waves that have a group velocity component in the x direction of 5 m s^{-1}. Also shown is the wind direction, the Δk_x corresponding to the spread over the three visible downwind peaks, and the boundaries of the directional filter used for Figs. 4–6 (solid, black lines, roughly ±60° about the wind direction).

$$T_x = \frac{L_x}{|\Delta c_x^g|} \quad \text{and} \quad T_y = \frac{L_y}{|\Delta c_y^g|}. \tag{5.4}$$

In the observed groups, the angle of the waves relative to the group envelope is less than 30° or so; thus, the contribution of κ_y to $|\kappa|$ (and to $|c^g|$) is less than half that of κ_x. Then, since $\Delta\kappa_y$ is about 5 times smaller than $\Delta\kappa_x$, the net effect of $\Delta\kappa_y$ on c^g should be roughly 1/10th that of $\Delta\kappa_x$, justifying its neglect. Thus, we assume the main cause of both Δc_x^g and Δc_y^g is the spread $\Delta\kappa_x$ in κ_x.

To estimate the effect of a spread $\Delta\kappa_x$ about a center component value κ_{x0}, we could Taylor expand from $\kappa_{x,0}$ to $\kappa_{x,0} \pm \frac{1}{2}\Delta\kappa_x$—the error in Δc_x^g keeping just the linear term should be of order 20%. However, adding this to the 10% error already incurred for ignoring $\Delta\kappa_y$ would make the result only marginally believable. Moreover, it is straightforward to compute the difference directly:

$$\Delta c_x^g = c_x^g\left(\kappa_{x,0} + \frac{1}{2}\Delta\kappa_x, \kappa_y\right) - c_x^g\left(\kappa_{x,0} - \frac{1}{2}\Delta\kappa_x, \kappa_y\right) \tag{5.5}$$

and

$$\Delta c_y^g = c_y^g\left(\kappa_{x,0} + \frac{1}{2}\Delta\kappa_x, \kappa_y\right) - c_y^g\left(\kappa_{x,0} - \frac{1}{2}\Delta\kappa_x, \kappa_y\right). \tag{5.6}$$

Here,

$$c_x^g = c^g\left(\frac{\kappa_x}{\kappa}\right) = c^g \frac{\kappa_{x,0} \pm \frac{1}{2}\Delta\kappa_x}{\left[\left(\kappa_{x,0} \pm \frac{1}{2}\Delta\kappa_x\right)^2 + \kappa_y^2\right]^{1/2}}, \tag{5.7}$$

$$c_y^g = c^g\left(\frac{\kappa_x}{\kappa}\right) = c^g\left\{\frac{\kappa_y}{\left[\left(\kappa_{x,0} \pm \frac{1}{2}\Delta\kappa_x\right)^2 + \kappa_y^2\right]^{1/2}}\right\}, \tag{5.8}$$

and

$$c^g = \frac{1}{2}\sqrt{\frac{g}{\kappa}} = \frac{1}{2}\sqrt{\frac{g}{\left[\left(\kappa_{x,0} \pm \frac{1}{2}\Delta\kappa_x\right)^2 + \kappa_y^2\right]^{1/2}}}, \tag{5.9}$$

where g is gravity, and advection by the mean current (which does not depend on κ) is ignored. To be useful, these have to be recast in terms of the prescribed variables: the center wave component angle φ and the

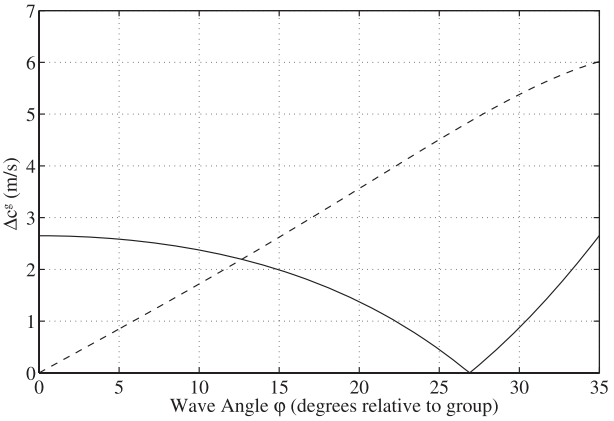

FIG. 8. The dispersal rates in the x and y directions (Δc_x^g; solid line, and Δc_y^g; dashed) due to the spread in the x component of wavenumber ($\Delta k_x \approx 2\pi/L_x$) vs slant-wave angle φ. Note that Δc_x^g goes to zero at about $\varphi = 27°$, at which point Δc_y^g is comparable to C (5 m s^{-1}), the x propagation speed of the groups.

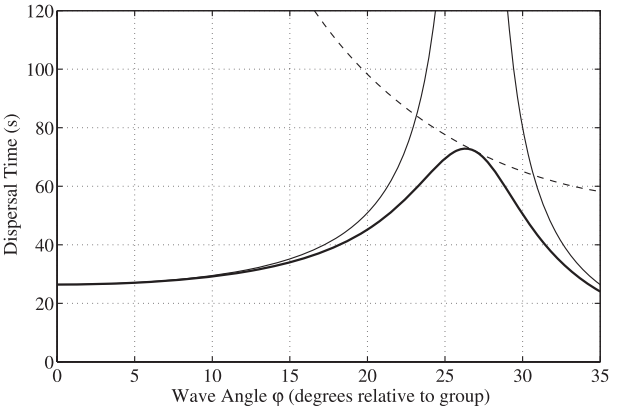

FIG. 9. The dispersal times in the x and y directions (T_x and T_y), and the net dispersal time for an elliptical group (T_d) vs slant-wave angle φ. The maximal net dispersal time is roughly set by the y dispersion $L_y/\Delta c_y^g$ at the angle where Δc_x^g goes to zero.

observed x-wise group speed $C = c_{x,0}^g = 5$ m s^{-1} (defined as fixed; note this applies to the center wavenumber: when displaced by $\frac{1}{2}\Delta\kappa_x$, the value will usually differ from this). The angle of propagation φ is defined as above, so 0° is upward (parallel to the x axis), with positive angles increasing counterclockwise, so +90° points along the $+y$ axis. Then, for the center wave component, $c_0^g = C/\cos\varphi$, $\kappa_0 = g/4(c_0^g)^2 = g\cos^2\varphi/4C^2$, so

$$\kappa_{x,0} = \kappa_0 \cos\varphi = \frac{g\cos^3\varphi}{4C^2} \tag{5.10}$$

and

$$\kappa_y = \kappa_0 \sin\varphi = \frac{g\cos^2\varphi\,\sin\varphi}{4C^2} \tag{5.11}$$

(note that the assigned spread $\Delta\kappa_x$ in κ_x is independent of the angle). Equations (5.10) and (5.11) describe the "roughly oval curve" shown in Fig. 7 (labeled "$c_x^g = 5$ m s^{-1},").

The results for Δc_x^g and Δc_y^g versus angle φ (with constant spread $\Delta\kappa_x = 2\pi/70$ m and $C = c_{x,0}^g = 5$ m s^{-1}) are shown in Fig. 8. A striking feature of this is that the x-wise dispersal Δc_x^g goes to zero at about 27° (actually 26.9°). At that angle, only the y dispersion acts to break the group up, so if it were infinitely long in the y direction it could persist indefinitely (a ship's wake is a good conceptual model of this limiting case). For this amount of spread $\Delta\kappa_x$, a rough rule of thumb is the spread in the x component Δc_x^g for $\varphi = 0°$ is about $\frac{1}{2}C$ (actually $0.53C$), and the spread in the y component Δc_x^g roughly equals C (actually $0.97C$) at the x component zero crossing angle $\varphi \approx 27°$ (but note these values change with $\Delta\kappa_x/|\kappa|$).

In general, both components of the group dispersal are involved, so we need to assign a shape to the model group to interpret cases where Δc_x^g and Δc_y^g are competitive. A reasonable and workable shape is an ellipse, with a major axis of length L_y parallel to the y axis and minor axis of length L_x. In this case, simply normalize the x and y ordinates by the respective group length scales:

$$x^* = \frac{x}{L_x} \quad \text{and} \quad y^* = \frac{y}{L_y}. \tag{5.12}$$

Then the normalized group boundary is a unit circle, and the dispersal time is just the time it takes the normalized spread in group velocity to go a unit distance in any direction:

$$\Delta c^* = (\Delta c_x^*,\ \Delta c_y^*) = \left(\frac{\Delta c_x^g}{L_x},\ \frac{\Delta c_y^g}{L_y}\right), \tag{5.13}$$

and the net dispersal time is

$$T_d = \frac{1}{|\Delta c^*|} = \frac{1}{[(\Delta c_x^g/L_x)^2 + (\Delta c_y^g/L_y)^2]^{1/2}} = (T_x^{-2} + T_y^{-2})^{-1/2}. \tag{5.14}$$

Figure 9 shows the dispersal times T_x, T_y, and T_d versus slant-wave angle φ for the case at hand ($C = 5$ m s^{-1}, $L_x = 70$ m, $L_y = 5L_x$). The longest net dispersal time T_d occurs very near the zero in Δc_x^g, so the time is essentially set by the value of Δc_y^g there. Using the "rule of thumb" values yields $L_y/C = 350/5 = 70$ s (or 10 wave periods), compared to the explicitly calculated maximum value of 72.9 s. For any case where $L_y \gg L_x$, then we can estimate the dispersal time as roughly L_y/C (for this amount of spread $\Delta\kappa_x$). In contrast, a collinear group would disperse in about $2L_x/C \approx 28$ s (or four periods), versus the explicitly calculated 26.4 s.

These dispersal estimates correspond to the time it takes a well-formed group (maximally compact) to disperse to something like twice the area. Since linear dynamics are time reversible, the time for the groups to coalesce would be the same, so the total estimated durations of each kind of group (from dispersed to compact to dispersed again) are twice the above. Considering this, a collinear group would endure for 8 wave periods, while the slant-wave group would persist for a bit over 20. The slant-wave group endurance is consistent with the observed group, which persists for 17 wave periods.

The fact that the phase speed of the waves comprising the group matches the wind speed suggests these are related to the wind. This leads to the questions ''when do such short persistent groups occur?'' and ''how frequently would one encounter them?'' To address these questions, we return to the group-forced response as a possible proxy measure.

6. Group-forced response and the occurrence of short persistent groups

Examination of these short, steep, and persistent wave groups was motivated by the study of Smith (2006b), which in turn was motivated by the occurrence of a distinctive ''ridge'' observed in the *k–f* spectra of surface velocities well away from the surface wave dispersion curve (e.g., as seen in Fig. 3). The ridge appears along a line corresponding to about 5 m s^{-1} on the *k–f* plane. Since wind waves with phase speeds matching the wind speed of 10 m s^{-1} would have group speeds of 5 m s^{-1}, Smith (2006b) was inspired to examine whether such wind wave groups were related to this variance. Smith (2006b) found that the physical location and strength associated with the ''5 m s^{-1} variance'' seen in the *k–f* spectra corresponds well with that of the waves' Stokes drift (though the response is larger than predicted by theory).

Here, we focus on the 5 m s^{-1} spectral ridge as a possible proxy for the occurrence of short, steep wave groups. The coherence between Stokes drift and the Eulerian response corresponding to this ridge was found by Smith (2006b) to be between -0.3 and -0.4, which is well above the 95% significance level. As we shall see, this level of coherence is consistent with a perfect ''signal'' correlation together with the expected Doppler noise of the velocity estimates for the configuration of the deployment. The correlation supports a one-to-one relation (actually -1 to 1) between the resolved wave-filtered Eulerian current response at the surface and the Stokes drift of the wave groups there (both minus the means). The length of the ridge on the *f–k* plane (Fig. 3) verifies both the shortness of the forcing groups (which sets the high-wavenumber cutoff) and the persistence (which sets the low-frequency cutoff). Note that consistent with the dynamics thought to play a part, this response emphasizes especially wave groups that are both steep and short. Since this ''5 m s^{-1} variance'' is easy to extract, we use it to assess how common such short persistent groups were over 9 days surrounding the observational segment shown. Visual inspection of a random sampling of these events on the full time-evolving 2D spatial plane verifies that the wave groups are similar, with the constituent waves at a finite angle (which varies a little) relative to the envelope of the group. The 9 days analyzed in this way encompass the example shown and have winds varying from 0 to 10 m s^{-1}.

Figure 10 shows the wave-filtered surface velocities for the case examined. A significant ''slash'' of negative velocity (current toward R/P *FLIP*) is located along the same line on the time–range plane as the short persistent surface wave group circled in Fig. 2, consistent with Smith's earlier finding (which was for a different data segment, on a different day than that shown here).

Based on these strong correlations, we conclude that the variance along the 5 m s^{-1} ridge in *k–f* spectra formed from each 8.5-min data segment is a reasonable proxy measure of the strength and frequency of the occurrence of compact persistent groups (we shall revisit this later). To estimate this variance, we mask the *k–f* spectrum over two separate 5 m s^{-1} bands, one going downwind (the proxy for short wave groups), and another going upwind (a ''control,'' since we expect no such upwind-propagating groups). Figure 11 shows an example of a *k–f* spectrum with outlines of the two masks.

The downwind mask (D5) and upwind mask (U5) were applied to the sequence of data files from 1430 HDT 26 September to 1725 HDT 4 October 2002. The results (Fig. 12) show D5 variances that correspond well with the wind, fading to near the noise floor when the wind is calm for a few hours, and rising shortly after the onset of 10 m s^{-1} winds.

Given the area of the masked region of the spectrum and the expected Doppler noise level, the estimated responses can be compared to the expected noise floor. The expected rms Doppler noise ΔV can be written in terms of the speed of sound c_s ($\approx$1540 m s^{-1}), the center frequency f_0 (50 kHz), the sample interval τ_s (0.1 ms), the length of the repeat sequence code L (23 samples), the number of samples averaged in range N_a (100), and the number of ''overlap samples'' $(M-1)L$, where M (=9) is the number of code repeats transmitted (Smith and Pinkel 1991):

$$\Delta V = \frac{c_s}{4\pi f_0 \tau_s}\left(\frac{1 + N_a/2N_0}{LN_aN_0}\right)^{1/2} \approx 4.25\,\mathrm{cm\,s^{-1}}. \qquad (6.1)$$

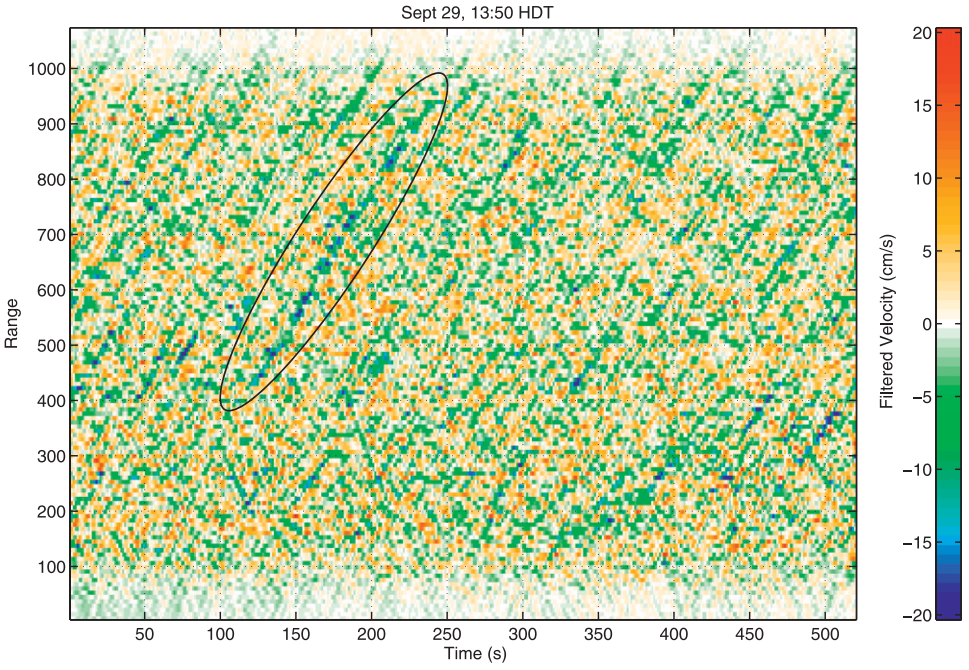

FIG. 10. *T–R* plot of the filtered (nonwave) surface velocities over the same *T–R* intervals as Fig. 2. The circled blue–green slash matches the location of the persistent wave group circled in Fig. 2. This is the surface signature of a forced response to the wave group, which is steep, short, and persistent. This kind of response produces the distinctive ridge of high variance in the corresponding *k–f* spectra along a straight line corresponding to a constant speed of roughly 5 m s^{-1} away from R/P *FLIP* (see Figs. 3 and 11).

Two further adjustments are needed: 1) in practice, the empirical noise variance is typically about double this value (increasing the rms by $2^{1/2}$), and 2) the received signal is filtered to 70% full bandwidth, which has the net effect of reducing L by a factor 0.7 in the above equation. The resulting adjusted estimate of the rms Doppler noise is 7.2 cm s^{-1}.

The D5 and U5 masks each capture about 1/25th of the total spectral area (actually 1331/32 768), so the Doppler noise is expected to contribute about 2.1 (cm s^{-1})^2. As seen in Fig. 12, this is consistent with both the D5 and U5 results over the first day or so, and then as the wind rises the ''control'' U5 increases to about 3, while the group-proxy D5 increases to between 4 and 7 (cm s^{-1})^2. Since some genuine surface activity (turbulence) is expected in the presence of wind, the indication is that the control U5 is a fair measure of the noise floor, and the difference D5 − U5 is a good measure of the group-forced response signal, as desired.

Overall, the downwind 5 m s^{-1} variance (D5) increases to about 2–4 (cm s^{-1})^2 larger than the control (U5) as the wind increases (to about 10 m s^{-1}). A delay is also seen, on the order of ½ a day between the wind rising and the response appearing. To check again on how well these proxy results match, we made a visual assessment of wave groups from a large selection of the *T–R* plots and found the correspondence to be quite good (as expected from the correlation and transfer function analysis): whenever D5 − U5 is bigger than 2 (cm s^{-1})^2 or so, there are short persistent groups evident in the *T–R* plots. Two ''spikes'' are seen in the estimates, one near 1800 HDT 26 September and the other near noon on 3 October. Upon examination, the latter appears to be a result of some very loud ambient noise, while the former, on the evening of 28 September, represents an exceptional collection of short, steep wave groups (see Fig. 13).

Next, we reconsider the coherence levels observed by Smith (2006b), with the spectral noise level estimate (from U5) in hand. The wave filter used in that analysis leaves intact about ⅔ of the spectral area (21 972/32 768 so the Doppler noise estimate yields a contribution of about 35 (cm s^{-1})^2, while the group-forced response estimate (D5 − U5) for that example yields about 4 (cm s^{-1})^2. Thus, the maximum coherence magnitude possible, even if the 4 (cm s^{-1})^2 signal were perfectly correlated with the waves' Stokes drift, would be only $(4/39)^{1/2} = 0.32$, which is consistent with the reported level. It appears that the true signals (wave-filtered response and Stokes drift variability) must be very tightly correlated indeed.

The typical contribution to D5 − U5, or ''5 m s^{-1} downwind variance,'' from the Eulerian wave group

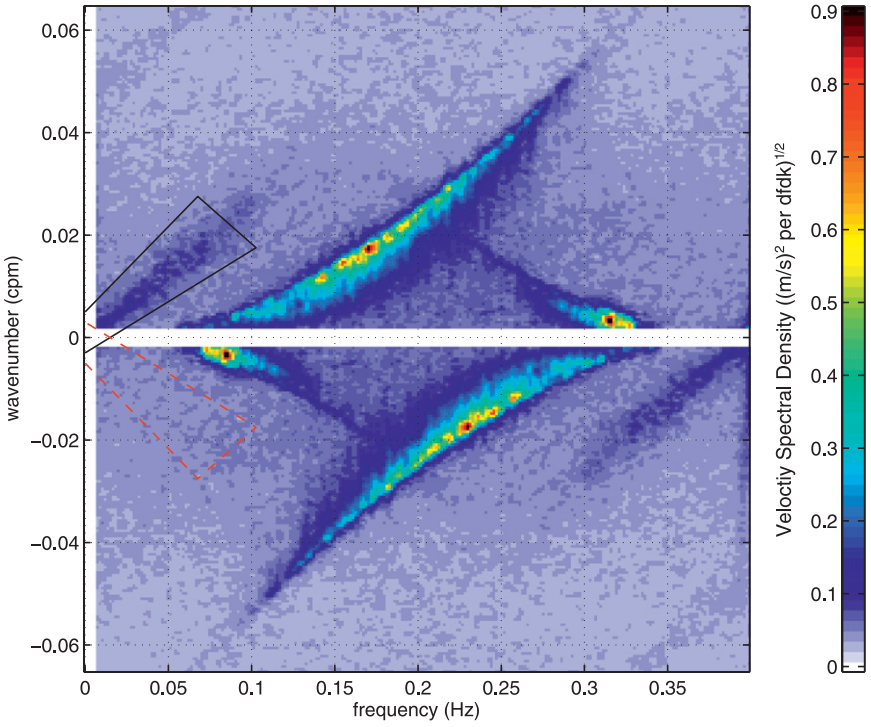

FIG. 11. The example *k–f* spectrum showing the two "5 m s^{-1}" masks. We focus on the region of the downwind-directed 5-m s^{-1} ridge (D5; black outline) as a proxy for the strength of the forcing wave groups in comparison to the control case (U5; red dashed), which selects upwind-directed responses and is expected to reflect the noise level of the spectral estimates. An especially strong group or several moderate ones may produce an equivalent signal. This spectral response emphasizes groups that are steep, short, and persistent.

responses in each data segment is about 3 (cm s^{-1})^2, while the actual "slashes" have velocities on the order of 10 cm s^{-1}; therefore, it appears that such a response is present about 1/33rd of the time. Since the duration of these groups is on the order of one wave period (=7 s), this would imply a group is typically encountered about once every 4 min or so. This is consistent with our visual estimate of 2–3 times per data segment (8.5 min); however, some segments have quite a few more (e.g., see Fig. 13), whereas others have none.

7. Discussion

The fact that the short persistent groups are only seen when the wind blows (~10 m s^{-1}, here) reinforces the idea that the waves involved are associated with the wind. For the wind direction encountered (blowing from the east), Oahu blocks waves coming from the southeast (see Fig. 1), so the longer waves are expected to be biased toward those going to the left of the wind direction (as shown in Fig. 7, the 2D wavenumber spectrum showing the direction toward). Shorter waves develop more quickly and hence are more nearly parallel to the wind. This wavelength directional "twist" is in the right sense to favor wave groups of the form seen, with a low-wavenumber peak to the left of the wind, a wind wave peak closer to the wind, and a higher-wavenumber peak continuing the trend. This is also a plausible explanation for the "handedness" of the observed groups—almost all have waves slanted in the sense of the example shown in detail (constituent waves oriented to the left of the direction of the envelope), and none were found oriented the other way. While upwind sheltering by an island or coast will certainly introduce this kind of spectral directional twist, it can also result from veering winds (e.g., as noted in Smith and Bullard 1995), so this condition can be met in open ocean conditions too.

The limiting case $L_y \to \infty$ is conceptually like one side of the wake of a boat that has moved at a constant speed in a straight line. We know the leading edge of such a wake (which makes a 19.5° angle with respect to the boat's path) remains well formed, with the largest wake waves confined to a narrow envelope near the leading edge (e.g., see Brown et al. 1989). The waves within the wake are oriented at an angle to the wake envelope, consistent with the present results. Naturally, the question arises of whether the observed persistent groups are remnants of actual ship

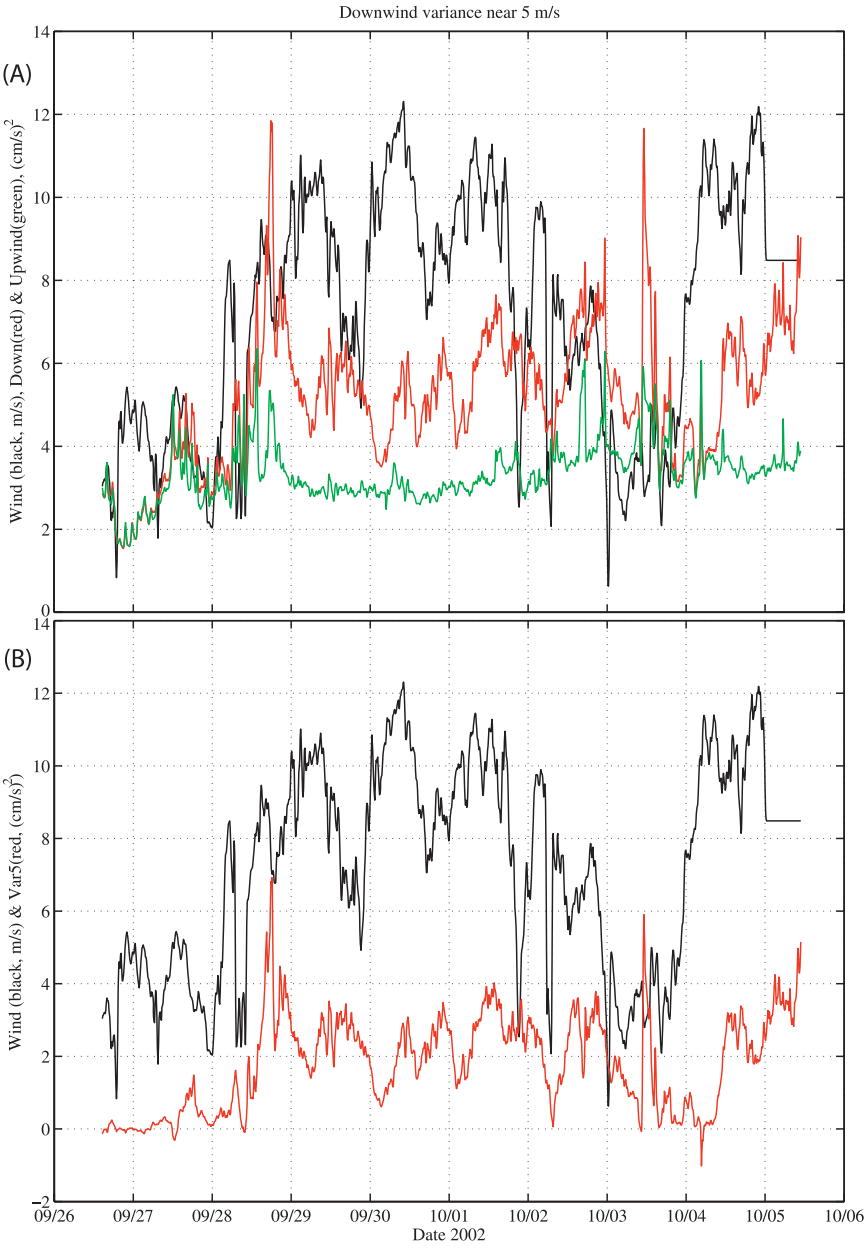

FIG. 12. (top) The wind (black), "downwind 5 m s^{-1} variance" (D5; red), and "upwind 5-m s^{-1} variance" (U5; green) over 9 days. At the start of this period, the wind was calm, and both D5 and U5 are near the expected noise level. Shortly after the wind rises, D5 increases more than U5 does. (bottom) Wind (black) and the difference (D5 − U5), thought to be a better indicator of the signal portion of the D5 variance. Correspondence with the wind is strong, with a delay on the order of ½ day. The highest peak in D5 − U5 occurs just after the wind rises, late on 28 September.

wakes. The angle of the wake to the ship track implies a ship speed about 3 times the speed of advance of the wake in the direction orthogonal to the wake's leading edge, so this would require ships going 15 m s^{-1}, which are rare. This high speed and the frequency of occurrence of such groups (see section 6) appear to rule this out. Also, the fact that the phase speed of the waves comprising the group matches the wind speed, and that they only appear when the wind is blowing, suggests that they are related to the wind, not shipping.

There a few ways these persistent wave groups may be important. 1) The unusually large group-forced response

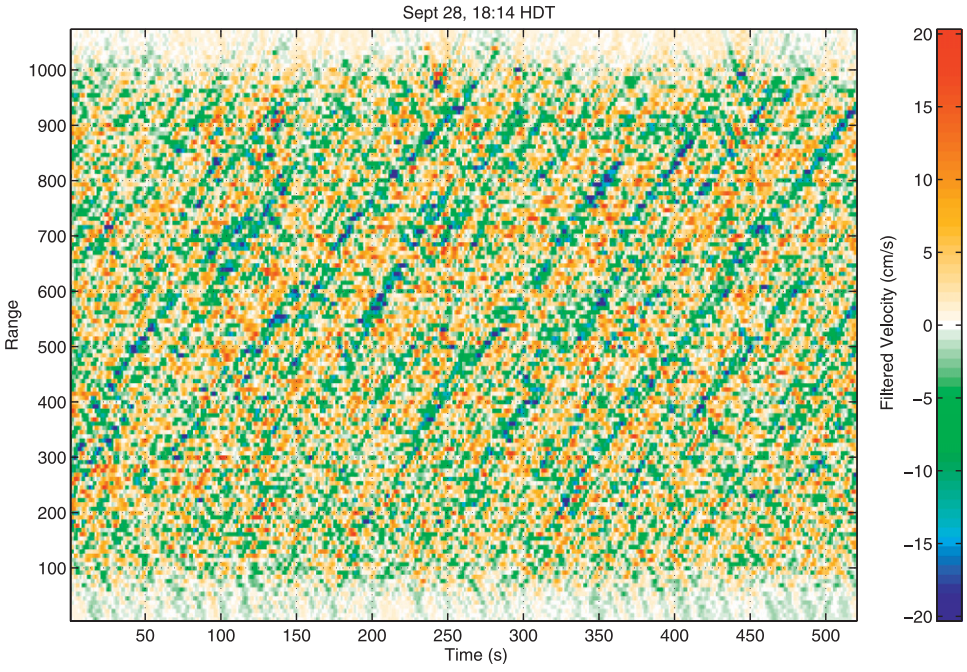

FIG. 13. *T–R* plot of the filtered (nonwave) surface velocity for the highest response segment, 1814 HDT 28 September. As indicated by the strength of the proxy measure (D5 − U5), there are many strong "forced group response" events, several lasting well over 100 s. The corresponding wave-velocity *T–R* plot shows a matching number of short, steep wave groups, which corroborates our interpretation (not shown for brevity).

has yet to be explained and could be of wider significance. 2) The waves in these groups are probably breaking, since they are among the steepest (though certainly many other waves are breaking as well, due to random superposition). The existence of a persistent line of breakers, with an envelope oriented some 20°–30° off the crosswind direction, could result in some large-scale interactions with the airflow. 3) Since the wave groups move at half the wind speed, we speculate there is potential for some kind of direct interaction with eddies in the atmospheric surface shear flow. 4) As noted by a reviewer, the slant-wave orientation also implies that breaking could happen continuously, as an individual wave crest maximum slips sideways along the group, rather than just breaking briefly as the wave crosses in the short direction. In this case, a mariner traveling at a corresponding angle to port of downwind might manage to keep up with the continually breaking crest, helping to either win a race or to capsize and cause trouble.

8. Conclusions

Persistent wave groups, propagating at about 5 m s^{-1}, were observed to occur frequently over the several days considered here, whenever the wind blew (the wind alternated between calm and about 10 m s^{-1} from the east). Linear propagation dynamics are sufficient to explain these observed groups. Very short groups, only one wavelength long, can persist as long or even longer than those observed—up to 20 wave periods for the group envelope geometry observed. The key to this persistence is that the waves composing the groups have crests oriented at an angle relative to the group envelope's major axis, which is much longer than the short direction.

Using previously noted group-forced responses (Smith 2006b) as a proxy for the occurrence of short, steep, and persistent wave groups, we assessed how often they occurred. Over the 9 days studied, winds rose from calm to 10 m s^{-1} twice. After the wind starts to blow, the group-forced response becomes distinct, and compact persistent groups similar to that described here were then encountered roughly 2–3 times per data segment (8.5 min), or 15–20 times h^{-1}. The delay after the onset of wind is on the order of ½ a day.

Acknowledgments. The field work and initial analysis was supported by ONR (N00014-02-1-0855), with additional analysis and modeling supported by NSF (OCE 06-23679). Thanks are due to the OPG engineering team of E. Slater, M. Goldin, M. Bui, and A. Aja for their tireless efforts to design, construct, deploy, and operate the LRPADS and help develop the software to acquire

and analyze the data, and to many others for many interesting and educational conversations.

REFERENCES

Banner, M. L., and W. L. Peirson, 2007: Wave breaking onset and strength for two-dimensional deep-water wave groups. *J. Fluid Mech.,* **585,** 93–115.

Bendat, J. S., and A. G. Piersol, 1986: *Random Data*. 2nd ed. John Wiley & Sons, 566 pp.

Benjamin, T. B., and J. E. Feir, 1967: The disintegration of wave trains on deep water. Part 1. Theory. *J. Fluid Mech.,* **27,** 417–430.

Brown, E. D., S. B. Buchsbaum, R. E. Hall, J. P. Penhune, K. F. Schmitt, K. M. Watson, and D. C. Wyatt, 1989: Observations of a nonlinear solitary wave packet in the Kelvin wake of a ship. *J. Fluid Mech.,* **204,** 263–293.

Crawford, C. B., and D. M. Farmer, 1987: On the spatial distribution of ocean bubbles. *J. Geophys. Res.,* **92,** 8231–8243.

Dysthe, K., 1979: Note on a modification to the non-linear Schrodinger-equation for application to deep-water waves. *Proc. Roy. Soc. London,* **369A,** 105–114.

——, H. E. Krogstad, and P. Muller, 2008: Oceanic rogue waves. *Annu. Rev. Fluid Mech.,* **40,** 287–310.

Hasselmann, K., and Coauthors, 1973: Measurements of wind-wave growth and swell decay during the Joint North Sea Wave Project (JONSWAP). *Dtsch. Hydrogr. Z.,* **80** (Suppl. A), 1–95.

Klymak, J. M., R. Pinkel, and L. Rainville, 2008: Direct breaking of the internal tide near topography: Kaena Ridge, Hawaii. *J. Phys. Oceanogr.,* **38,** 380–399.

Longuet-Higgins, M. S., 1978: Instabilities of gravity-waves of finite-amplitude in deep water. 2. Subharmonics. *Proc. Roy. Soc. London,* **360A,** 489–505.

——, and R. W. Stewart, 1962: Radiation stress and mass transport in gravity waves, with application to 'surf-beats'. *J. Fluid Mech.,* **13,** 481–504.

Phillips, O. M., 1958: The equilibrium range in the spectrum of wind-generated ocean waves. *J. Fluid Mech.,* **4,** 426–434.

Pinkel, R., and J. A. Smith, 1992: Repeat-sequence coding for improved precision of Doppler sonar and sodar. *J. Atmos. Oceanic Technol.,* **9,** 149–163.

——, and D. Rudnick, 2006: Hawaii Ocean Mixing Experiment (HOME). *J. Phys. Oceanogr.,* **36,** 965–966.

Rummler, W. D., 1968: Introduction of a new estimator for velocity spectral parameters. AT&T Bell Labs. Rep. MM-68-4141-5, 24 pp.

Smith, J. A., 2002: Continuous time–space sampling of near-surface velocities using sound. *J. Atmos. Oceanic Technol.,* **19,** 1860–1872.

——, 2006a: Wave–current interactions in finite depth. *J. Phys. Oceanogr.,* **36,** 1403–1419.

——, 2006b: Observed variability of ocean wave stokes drift, and the Eulerian response to passing groups. *J. Phys. Oceanogr.,* **36,** 1381–1402.

——, 2008: Vorticity and divergence of surface velocities near shore. *J. Phys. Oceanogr.,* **38,** 1450–1468.

——, and R. Pinkel, 1991: Improvement of Doppler estimation through repeat sequence coding. *Proc. Oceans '91: USA/ Ocean Technologies and Opportunities in the Pacific for the 90's,* Honolulu, HI, Institute of Electrical and Electronics Engineers, 977–984.

——, and G. T. Bullard, 1995: Directional surface wave estimates from Doppler sonar data. *J. Atmos. Oceanic Technol.,* **12,** 617–632.

Stokes, G. G., 1847: On the theory of oscillatory waves. *Trans. Cambridge Philos. Soc.,* **8,** 441–455.

Thorpe, S. A., 1986: Bubble clouds: A review of their detection by sonar, of related models, and of how Kv may be determined. *Oceanic Whitecaps and Their Role in Air–Sea Exchange Processes,* E. C. Monahan and G. Mac Niocaill, Eds., Springer, 57–68.

Tulin, M. P., and T. Waseda, 1999: Laboratory observations of wave group evolution, including breaking effects. *J. Fluid Mech.,* **378,** 197–232.

Whitham, G. B., 1974: *Linear and Nonlinear Waves*. Wiley-Interscience, 636 pp.